Journal of Materials Processing Tech. 345 (2025) 119064

Contents lists available at ScienceDirect

Journal of Materials Processing Tech.

journal homepage: www.elsevier.com/locate/jmatprotec

Research Article

# Achieving high-strength joining with superior metallurgical bonding in tungsten/steel via in-situ element-selective directional diffusion

Huaqi Xu [a,b], Wenjing Zhang [c], Xiaonan Qi [c], Wanjing Wang [a,b,*], Ji-Chao Wang [d,**], Ye Jiao [c], Kailun Li [e], Shubo Zhang [c], Mingshen Li [c], Yuping Xu [a,b], Haishan Zhou [a,b], Ming-Hsien Lee [f], Wei Liu [c,**], Guangnan Luo [a,b]

[a] Institute of Plasma Physics, Hefei Institutes of Physical Science, Chinese Academy of Sciences, Hefei 230031, China
[b] University of Science and Technology of China, Hefei 230026, China
[c] School of Materials Science and Engineering, Tsinghua University, Beijing 100084, China
[d] Institute of Energy, Hefei Comprehensive National Science Center, Hefei Anhui, 230031China
[e] Institute of Engineering Thermophysics, Chinese Academy of Sciences, Beijing 100190, China
[f] Department of Physics, Tamkang University, Department of Physics, 25137, Taiwan

ARTICLE INFO

*Keywords:*
Tungsten
RFAM steel
Joint
Metallurgical bonding
Brittle phase modification
Interfacial elemental diffusion
Reticulate heterostructure

ABSTRACT

To address the weak metallurgical bonding at interfaces in traditional tungsten (W)/steel joints with copper (Cu) interlayers, this study proposes a strategy of in-situ element-selective directional diffusion, achieving high-strength metallurgical transition bonding at both W/Cu and Cu/steel interfaces. Specifically, by introducing a Cu-Ge interlayer at the W/steel interface, multi-physics-driven forces (gravity and temperature fields) were utilized to enable the selective directional diffusion of Fe and Cr from the steel across the Cu-based interlayer. These elements migrated through the Cu interlayer, forming an Fe-rich deposition layer at the W/Cu interface, realizing a metallurgically bonded W/Fe/Cu transition. Furthermore, compared to the brittle $Fe_2W$ phase typically formed at conventional W/Fe interfaces, this study achieved in-situ toughening of the $Fe_2W$ phase through lattice distortion and stacking faults engineering. Simultaneously, the entire distribution of Cu along steel grain boundaries formed a discontinuous reticulate Cu/steel heterostructure, effectively addressing the low bonding strength of conventional Cu/steel interfaces. Ultimately, an unprecedented shear strength of 380 MPa was attained. This work elucidates the mechanisms of interfacial metallurgical bonding, strengthening, and in-situ modification of brittle phases in dissimilar metal joints with significant thermophysical property differences. It provides a novel pathway for high-strength metallurgical joining of dissimilar metals in harsh service environments and offers new insights into the modification and toughening of brittle phases at welded interfaces.

## 1. Introduction

Nuclear fusion energy represents a pivotal solution to global energy challenges, owing to its inherent safety, efficiency, resource abundance, and environmental cleanliness [1]. Within fusion devices, breeder blankets perform critical functions such as tritium breeding, energy extraction and radiation shielding [2]. First-wall components of breeder blankets integrate tungsten (W) as plasma-facing materials (PFMs), and reduced-activation ferritic/martensitic steel (RAFMS) as structural materials [3]. However, joining W to steel presents fundamental challenges. The absence of W-Fe thermodynamic equilibrium prevents single-phase solid solution formation [4], leading to brittle intermetallic compounds (IMCs) such as $Fe_2W$ at the interface [5]. In addition, severe coefficient of thermal expansion (CTE) mismatch induces significant thermal stress concentration during post-fabrication cooling [6]. Synergistic $Fe_2W$ embrittlement and interfacial thermal stress promote cracking susceptibility [7]. Particularly under operational fusion conditions, W-steel joints experience concurrent high-heat fluxes and high-energy neutron irradiation [8], imposing extreme demands on joints performance.

To mitigate cracking in direct W/steel joining, conventional approaches employ interlayers to release thermal stress. Interlayers such as

* Corresponding author at: Institute of Plasma Physics, Hefei Institutes of Physical Science, Chinese Academy of Sciences, Hefei 230031, China.
** Corresponding authors.
*E-mail addresses:* wjwang@ipp.ac.cn (W. Wang), wangjc@ie.ah.cn (J.-C. Wang), liuw@mail.tsinghua.edu.cn (W. Liu).

https://doi.org/10.1016/j.jmatprotec.2025.119064
Received 30 May 2025; Received in revised form 6 September 2025; Accepted 7 September 2025
Available online 8 September 2025

Ni, Zr, Ti [9], with CTE values intermediate to W and steel, partially alleviate thermal stress. However, these often form brittle IMCs with the base metals, compromising joint strength. In contrast, Cu interlayers, owing to their exceptional plastic deformation capacity and absence of brittle phase formation with W or steel, emerge as an ideal candidate [10]. Yet, the near immiscibility of W and Cu results in non-alloyed interfaces, leading to poor metallurgical bonding and low joint strength [11].

To enhance joint strength and achieve robust metallurgical bonding at the W/Cu interface, composite interlayers have been explored. For instance, Zhang et al. [12] and Wang et al. [9] introduced Zr or Ti interlayers at the W/Cu interface, creating W-Zr-Cu-steel or W-Ti-Cu-steel joints that improved metallurgical bonding. Nevertheless, elemental diffusion in these structure formed brittle IMCs (e.g., Zr-Cu [12], Ti-Fe [9]), severely degrading strength of joints. Thus, adding extra interlayers introduces new challenges while increasing manufacturing complexity and cost for blanket components [13].

Therefore, the key to solving this problem lies in how to in-situ form a transition layer at the W/Cu interface using the existing elements within joint to achieving W/transition layer/Cu metallurgical bonding. Fe, present in substantial quantities within the joint and capable of forming metallurgical interfaces with both Cu and W, serves as the optimal candidate. However, the Fe-Cu exhibits limited solid solubility with insufficient intrinsic diffusion driving force [14]. To overcome this limitation, it is essential to provide an adequate driving force to facilitate Fe diffusion across the Cu interlayer and deposition on the W side. According to the Cu-Ge and Fe-Ge binary phase diagrams, germanium (Ge) effectively reduces solid-liquid transition temperature of Cu, which is beneficial for reducing the activation energy for Cu-steel interdiffusion, enhancing reactive wettability of Cu to steel and promoting their interdiffusion [15]. Concurrently, Ge exhibits excellent solid solubility with Fe, which can further enhance solubility of Fe in liquid Cu phase [16]. Moreover, the low solid solubility between Cu and Fe permits density-driven migration of Fe across the Cu interlayer to deposit on the W side rather than dissolve in the liquid Cu phase. Additionally, based on the mechanism of chemical sedimentation that separates solid and liquid phases by gravity and the difference in component densities [17], Fe atoms with a density ($< 7.86$ g/cm$^3$) lower than that of Cu (8.960 g/cm$^3$) may be separated from the Cu melt and directionally deposited on the W side with the impact of gravity and temperature field [18]. This process was called in-situ element-selective directional diffusion. Thus, the W/Cu metallurgical bonding can be achieved by in-situ formation of an Fe-rich directional deposition layer between W and Cu. However, direct W-Fe contact risks forming brittle $Fe_2W$ phases, resulting in low interfacial strength. Therefore, while achieving metallurgical W-Fe-Cu-steel joints, the brittle $Fe_2W$ needs to be avoided. Zhang et al. effectively inhibited the formation of brittle TiCuSi IMCs by incorporating a reticulate structure to spatially divide the $Ti_3SiC_2$/-$Ti_2AlNb$ interface [19]. Chen et al. successfully suppressed the formation of the brittle $Mg_2Si$ IMCs at the Mg/Al interface through controlling elemental redistribution [20]. Therefore, in this study, achieving $Fe_2W$ modification may be feasible by adjusting the interface structure and the IMCs composition, thereby ensuring a high-strength W/Fe bonding.

In summary, on the basis of the traditional Cu-based interlayer, how to achieve a robust W/steel metallurgical bonding by utilizing the directional diffusion of existing elements in the joint and modifying the interfacial brittle phase without introducing an additional new interlayer remains the core challenge. Therefore, this work proposes an innovative strategy of element-selective directional diffusion. This work elucidates the mechanisms of interfacial metallurgical bonding, strengthening and in-situ modification of brittle phases in dissimilar metal joints with significant thermophysical property differences. It provides a novel pathway for high-strength metallurgical joining of dissimilar metals in harsh service environments and offers new insights into the modification and toughening of brittle phases at welded interfaces.

## 2. Experimental and computational procedure

### 2.1. Experimental materials

The experimental materials used in this study are as follows: I. W plates (purity 99.95 wt%) provided by Advanced Technology & Materials Co. Ltd (AT&M). II. The Chinese Low Activation Ferritic/Martensitic (CLF-1) steel (8.5 Cr, 0.098 C, $\geq$ 0.03 Al, 0.60 Mn, 0.034 N, 0.29 V, 0.038 Ta and balance Fe, wt%) provided by the YUANFANG High-Tech Equipment Parts Co. Ltd. III. The Cu-Ge filler, 11.5–12.5 % Ge, with the melting temperature 850 $\pm$ 10 ℃, was provided by the CNMC Shenyang Research Institute of Nonferrous Metals Co. Ltd. IV. Metallographic samples were etched using a $FeCl_3$-HCl solution composed of 20 g $FeCl_3$, 30 ml HCl, and 100 ml $H_2O$.

### 2.2. Experimental procedures

Before samples were assembled, the surfaces of W and steel substrates to be joined were ground and polished to achieve a surface roughness of less than 0.8 μm, ensuring clean and flat interfaces. Subsequently, two joints with distinct structural configurations were employed for assembly: the symmetric joint was assembled in a top-down manner as steel / Cu-Ge filler / W / Cu-Ge filler / steel, as shown in Fig. 1(a), aiming to evaluate the feasibility of in-situ formation of Fe-rich interlayers and investigate their formation mechanism; the single-sided joint had a structure of W / Cu-Ge filler / steel, as shown in Fig. 1(b), which was used for micro-characterization and shear performance evaluation. To ensure reliable contact between the substrate and filler, mechanical clamping is applied to the assembled components. All assembled specimens were placed within a vacuum furnace maintained at $10^{-3}$ Pa. The brazing cycle comprised heating to 1040°C at 10 °C/min, followed by an isothermal hold to ensure the fluidity of Cu-Ge filler. The symmetric joints were held for 10 min at 1040 ℃, while the single-sided joints were held for 1, 2, or 3 h at 1040 ℃. Finally, all the samples were cooled at a rate of 10 °C/min. Temperature profiles throughout the brazing cycles were monitored in real-time using thermocouples, as shown in Fig. 1(c).

### 2.3. Characterization methods

The microstructure of joints was observed using a field emission scanning electron microscope (FE-SEM, ZEISS) equipped with an electron back-scattered diffraction (EBSD) and an energy-dispersive X-ray spectrometer (EDS). An electron Probe X-ray micro analyzer (EPMA, JEOL, JXA-8230) was used to observe the elemental distribution of joints. Transmission electron microscopy (TEM) specimens of the W/Fe interface were prepared using a dual-beam focused ion beam scanning electron microscope (FIB-SEM, Helios G4 UX) and subsequently examined using a TEM (JEOL F200). TEM analysis was conducted by a bright-field (BF), dark-field (DF) and scanning transmission electron microscopy (STEM) equipped with a high-angle annular dark field (HAADF) and a STEM energy dispersive X-ray spectroscopy (EDS). Interfacial phase identification was conducted by a selected-area electron diffraction (SAED) and a high-resolution transmission electron microscopy (HRTEM). The hardness distribution of joints was measured using a Wilson Vickers Hardness tester (VH3100). Moreover, the primary cracking type of W/steel joints after the high heat flux fatigue test (simulating nuclear fusion conditions) was the sliding mode crack (II type) [21]. Thus, it is important to evaluate and improve the shear performance of W/steel joints. In this study, shear testing was conducted in accordance with the standard YS/T 485–2005, with corresponding schematic diagrams of the shear sample and clamp setup provided in Fig. 1(d).

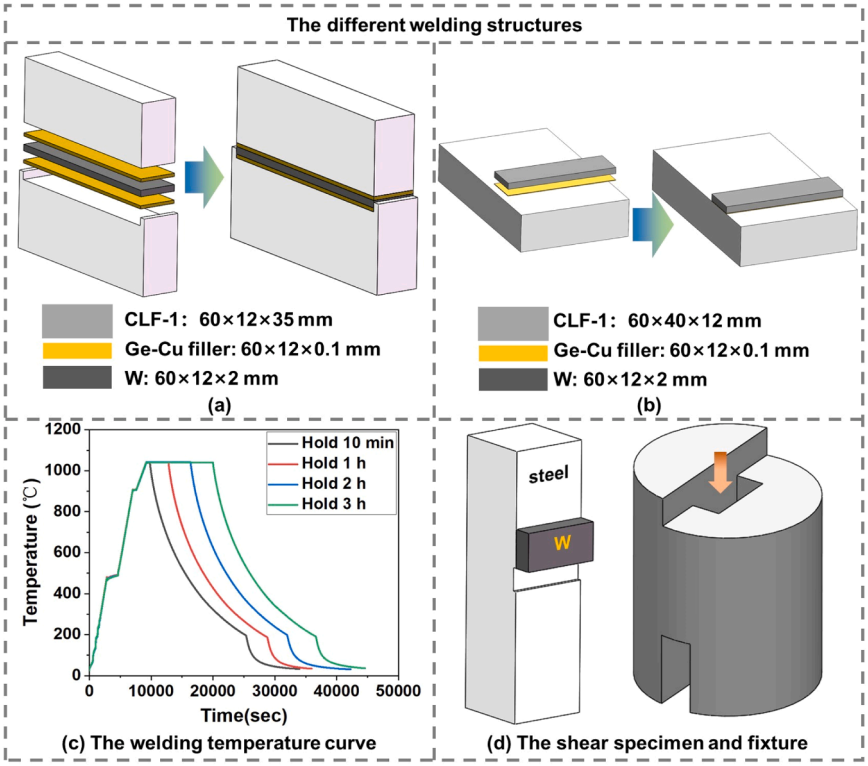


**Fig. 1.** (a-b) Schematic diagrams of different structures before and after assembly: (a) the symmetric welding structure, (b) the single-side welding structure. (c) Complete temperature change curves recorded during various holding periods using thermocouples. (d) Schematic diagrams of the uniaxial compression shear specimen and clamp setup (specific dimensions are shown in Fig. S1).

### 2.4. First-principles calculation and finite element models methods

The experimental design aimed to form a Fe-rich deposition layer to establish metallurgical W/Fe and Fe/Cu interfaces, rather than an unalloyed W/Cu interface, it is essential to determine the relative reactivity and bonding stability of W base metal with Fe or Cu. Therefore, the binding energies and charge differential densities of the W/Cu and W/Fe interface to reflect the interatomic bonding strength and interfacial stability were calculated using first-principles calculations. The calculation was based on density functional theory (DFT) using the CASTEP code within the generalized gradient approximation (GGA) [22]. In accordance with the principle that lower energy corresponds to greater structural stability [23], interface models with lowest energy were selected as bonding surfaces [24]. The crystal orientation combination of $(100)_W$ - $(100)_{Fe}$ and $(110)_W$ - $(111)_{Cu}$ had the lowest interfacial energy [25]. The atomic layers thicknesses of the W, Fe, and Cu unit cells in this study were determined based on the number of layers used in existing literature for investigating interfacial properties [26,27]. Previous studies have demonstrated that even with fewer atomic layers and a smaller total number of atoms than those used in this work, sufficiently accurate computational results can be obtained. Two interface models were constructed as shown in Fig. 2(a) and (b). The total energy, interfacial energy, formation energy and charge density difference of two interface models were calculated respectively. The computational parameters were set as follows: the kinetic energy cut-off was 400 eV with 300 eV already achieving convergence within 0.1 eV/atom for this system, thereby ensuring full structural relaxation, the k-point sampling for supercells was 3 × 3 × 1, the lattice parameters a, b, and c of interface models were summarized in Table 1. Consistent computational parameters were applied for both geometric optimization and total energy calculation across all interfaces. To construct the most stable interface models for biphasic crystal planes, variations in atomic count and layer thickness between the two interface models render direct comparison of their total energy infeasible. Instead, the interface binding energy was computed using Eq. (1) [28]:

$$W_{ab\ interface} = \frac{1}{A}(\gamma_{ab\ interface} - \gamma_a - \gamma_b) \quad (1)$$

Wherein $\gamma_a$ and $\gamma_b$ are the energy of the surface $a$ and $b$, $\gamma_{ab\ interface}$ is the total interface energy, and $W_{ab\ interface}$ is the interface binding energy, A is the interface area.

In addition, finite element simulations were performed to verify the distribution of residual stress and strain in W-steel joints, considering configurations both with and without Cu and Fe interlayers of varying thicknesses. The distribution of residual stress and strain in W-steel joints with or without Cu layers and Fe layers of different thicknesses was verified by finite element simulation. Corresponding finite element models are shown in Fig. 2(c) and Fig. 2(d), with relevant thermophysical parameters detailed in Fig. S2 and Fig. S3. To ensure the accuracy of computational results, the dimensions of simulated joints were scaled up by a factor of ten [29].

## 3. Results

### 3.1. Computational results

As shown in Table 2, the total interface energy and interface binding energy of the $(100)_W$ - $(100)_{Fe}$ and $(110)_W$ - $(111)_{Cu}$ interface were calculated by Eq. (1). Compared to the $(110)_W$ - $(111)_{Cu}$ interface with binding energy of $-0.225$ eV/Å$^2$, the $(100)_W$ - $(100)_{Fe}$ interface exhibited a lower potential energy with a binding energy of $-0.567$ eV/Å$^2$. This lower energy state indicated greater thermodynamic stability and stronger interfacial bonding in the W-Fe interface. Additionally, the interfacial charge density difference distributions were calculated, as presented in Fig. 3(a) and Fig. 3(c), blue regions denoted electron depletion, while red regions indicated electron accumulation. Analysis

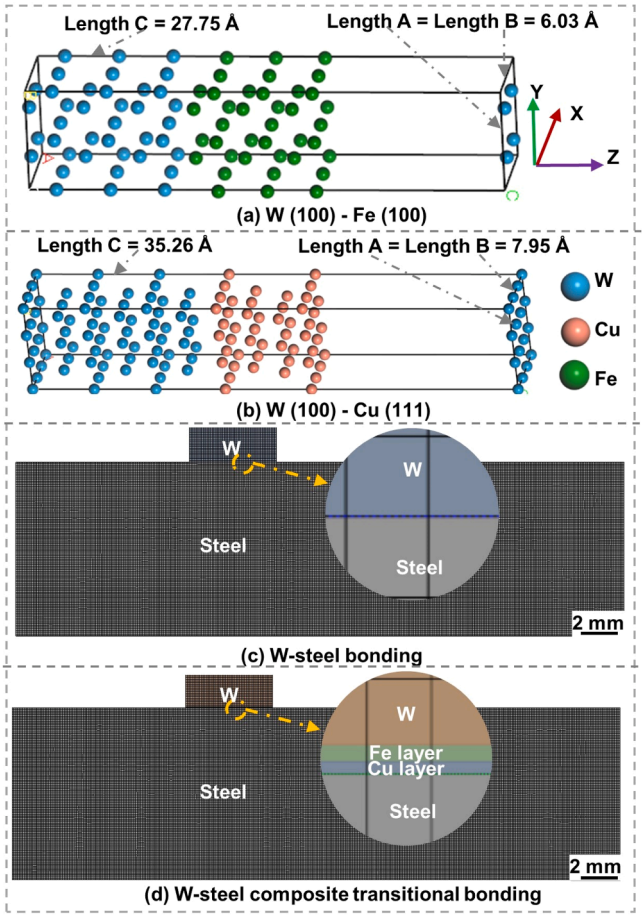


**Fig. 2.** Models employed in first-principles calculations and finite element simulations. (a) $(100)_W$ - $(100)_{Fe}$ interface model, (b) $(110)_W$ - $(111)_{Cu}$ interface model, (c) the W/steel joint without interlayers, and (d) the W/steel joint incorporating both Fe and Cu interlayer.

**Table 1**
The lattice parameters of different interface models.

| Interface model | Lattice parameter | | |
|---|---|---|---|
| | a | b | c |
| **W-Fe interface** | 6.03 Å | 6.03 Å | 27.75 Å |
| **W-Cu interface** | 8.09 Å | 8.09 Å | 33.24 Å |

**Table 2**
W/Fe and W/Cu interface binding energy.

| Interface system | Interface binding energy (eV/Å$^2$) |
|---|---|
| $(100)_W$ - $(100)_{Fe}$ | −0.567 |
| $(110)_W$ - $(111)_{Cu}$ | −0.225 |

along the fitted slice directions in Fig. 3(b) and Fig. 3(d) revealed significantly greater electron density accumulation at the W-Fe interface compared to the W-Cu interface. These observations demonstrated that W atoms preferentially reacted and established a more stable alloyed interface with Fe atoms rather than Cu atoms.

Fig. 4 presents the stress and strain distribution of different W/steel joints calculated by finite element numerical simulation. The W/steel directly joint without interlayers exhibited pronounced residual stress concentrations and localized strain accumulation at the interface in Fig. 4(a-b1). Conversely, the W/steel joint with Cu and Fe interlayers showed substantially reduced peak stress and strain magnitudes at the

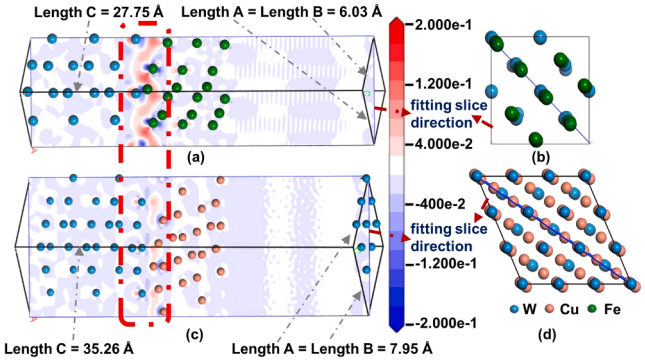


**Fig. 3.** Charge density difference of (a) the W-Fe interface and (c) the W-Cu interface. The fitting slice direction of (b) the W-Fe interface and (d) the W-Cu interface.

interface in Fig. 4(c-d1). Quantitative analysis across varying interlayer thicknesses demonstrated that both peak residual stress and equivalent strain decreased significantly with increasing Cu and Fe interlayer thickness in Fig. S4. This thickness-dependent mitigation effect was visually apparent in the residual stress and strain contour plots in Fig. 4 (e) and Fig. 4(f), confirming that Cu and Fe interlayers were essential for minimizing interfacial stress concentrations.

### 3.2. Experimental results

The SEM images of the symmetric joint held 10 min are shown in Fig. 5(a-b1). Analysis of the W/steel interface beneath the W substrate revealed distinct regions: the W base metal, the W/Fe interface, the Fe-rich deposition layer, the Cu-based layer, the Cu/steel interface, and ferrite and martensite base metal. No cracks were observed within these interfacial regions. Quantitative EMPA point scans revealed the atomic ratio for 79.78Fe-8.70Cr-8.17Ge-0.88W-1.16Cu-1.31 C of the Fe-rich deposition layer and 4.67Fe-0.41Cr-0.40Ge-0.08W-92.54Cu-1.90 C of the Cu-based layer. This compositional profile demonstrated diffusion of Fe and Cr from the steel across the Cu-based interlayer, deposited on the W side along with Cu and Ge, as shown in Fig. 5(b). This process was called in-situ element-selective directional diffusion. Crucially, this Fe-rich layer established a metallurgically bonded W/Cu interface, effectively addressing the issue of non-metallurgically bonded W/Cu interface. Furthermore, Fig. 5(b1) shows the formation of serrated IMCs at the W/Fe interface. Quantitative EMPA point scans revealed the atomic ratio for 54.67Fe-8.09Cr-6.59Ge-29.52W-1.14Cu of the serrated IMCs, which meant that other elements have micro-alloyed within $Fe_2W$. In contrast, the W/steel interface above the W substrate in Fig. 5(a) and (a1) exhibited no Fe-rich deposition layer formed at cracked W/Cu interface. This direct comparison confirmed that the Fe-rich layer was essential for establishing crack-free W/Cu metallurgical bonding. The single-sided joints and their W/Fe interfaces held different time are shown in Fig. 5(c-e1). Corresponding EPMA elemental distribution maps are shown in Fig. 6. As holding time increased, the Fe-rich deposition layer thickened from 7.5 μm to 24 μm. Following solidification of the molten Cu-Ge filler, a reticular structure formed at the Cu/steel interface, with Cu distributing along steel grain boundaries in Fig. 6. Moreover, petal-like or particulate Fe-rich secondary phases identified by EPMA point analysis were precipitated in the Cu interlayer under insufficient holding time in Fig. 5(c2). These features signified incomplete directional diffusion of samples held 1 and 2 h. This was also the evidence that Fe atoms underwent directional diffusion across the Cu-based interlayer. With extended holding time, intensified Cu-Fe interdiffusion promoted significant liquid Cu penetration along steel grain boundaries. Ultimately, this generated a continuous Cu-steel reticular heterostructure in Fig. 5(e) and Figs. 6(c-c4), which was beneficial to localized direct bonding between the steel matrix and Fe-rich deposition

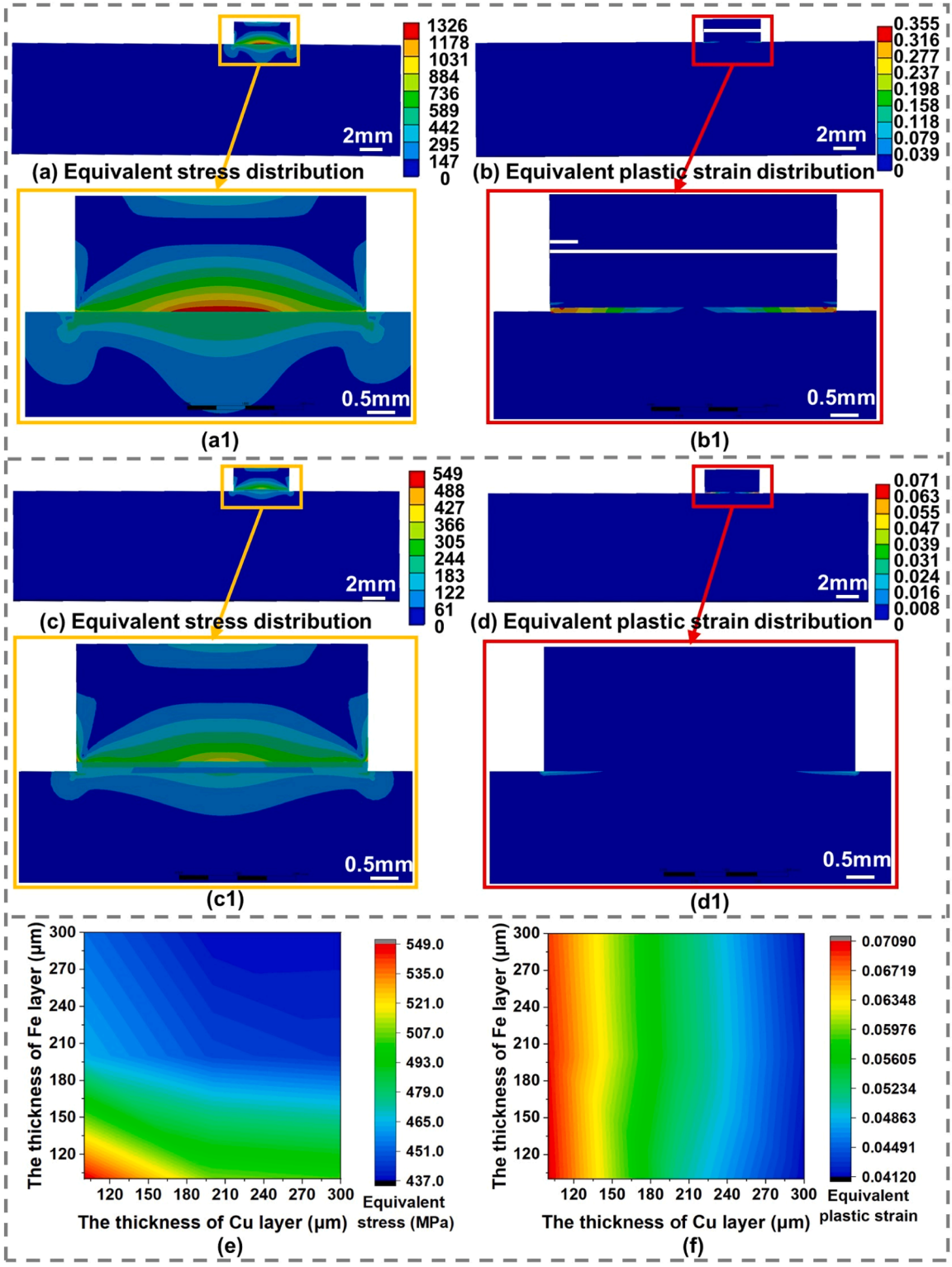


**Fig. 4.** The stress and strain distribution of different W/steel joints from finite element simulation. (a, a1) Stress distributions and (b, b1) strain distributions of W/steel joints without interlayers. (c, c1) Stress distributions and (d, d1) strain distributions of W/steel joints with Cu and Fe interlayers added. (e) Stress distribution cloud map and (f) strain distribution cloud map of W/steel joints with Cu and Fe interlayers of varying thicknesses.

layer.

The EBSD analyses of single-side joints held 1, 2 and 3 h are shown in Fig. 7. The EBSD results of the W/steel joint beneath the W substrate revealed a microstructure consisting of: elongated grain boundaries along the rolling direction in the W base metal, the W/Fe interface, an Fe-rich deposited layer with columnar grain morphology, a resolidified Cu layer, the Cu/Fe interface, as well as the ferritic and martensitic base metal regions. As the holding time increased, the thickness of the Fe-rich deposited layer grew, while the Cu layer transitioned from a single layered structure (under holding 1 h and 2 h) to a continuous Cu-steel reticular heterostructure (under holding 3 h). In contrast, grain growth in the base metal region was not significant. These observations

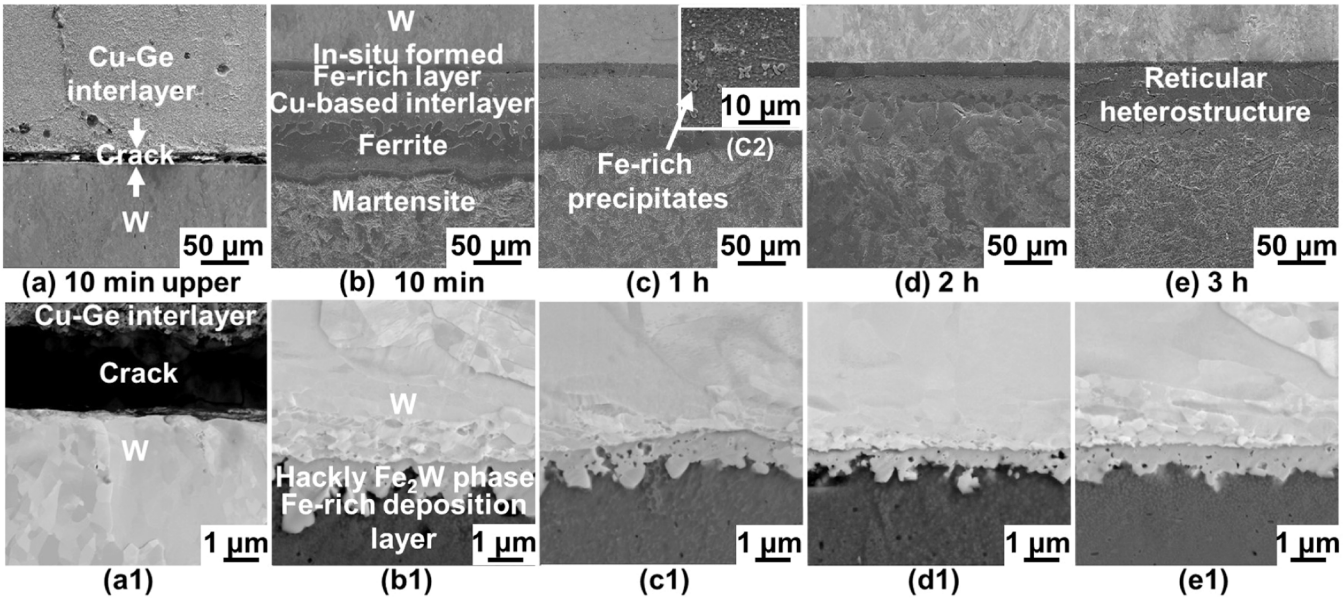


**Fig. 5.** Secondary electron SEM micrographs for different samples. (a) The upper half interface and (b) the lower half interface of the symmetric joint held 10 min. The interface of the single-side joints held (c) 1 h, (d) 2 h and (e) 3 h. (a1-e1) Enlarged view of the corresponding W/Fe interface.

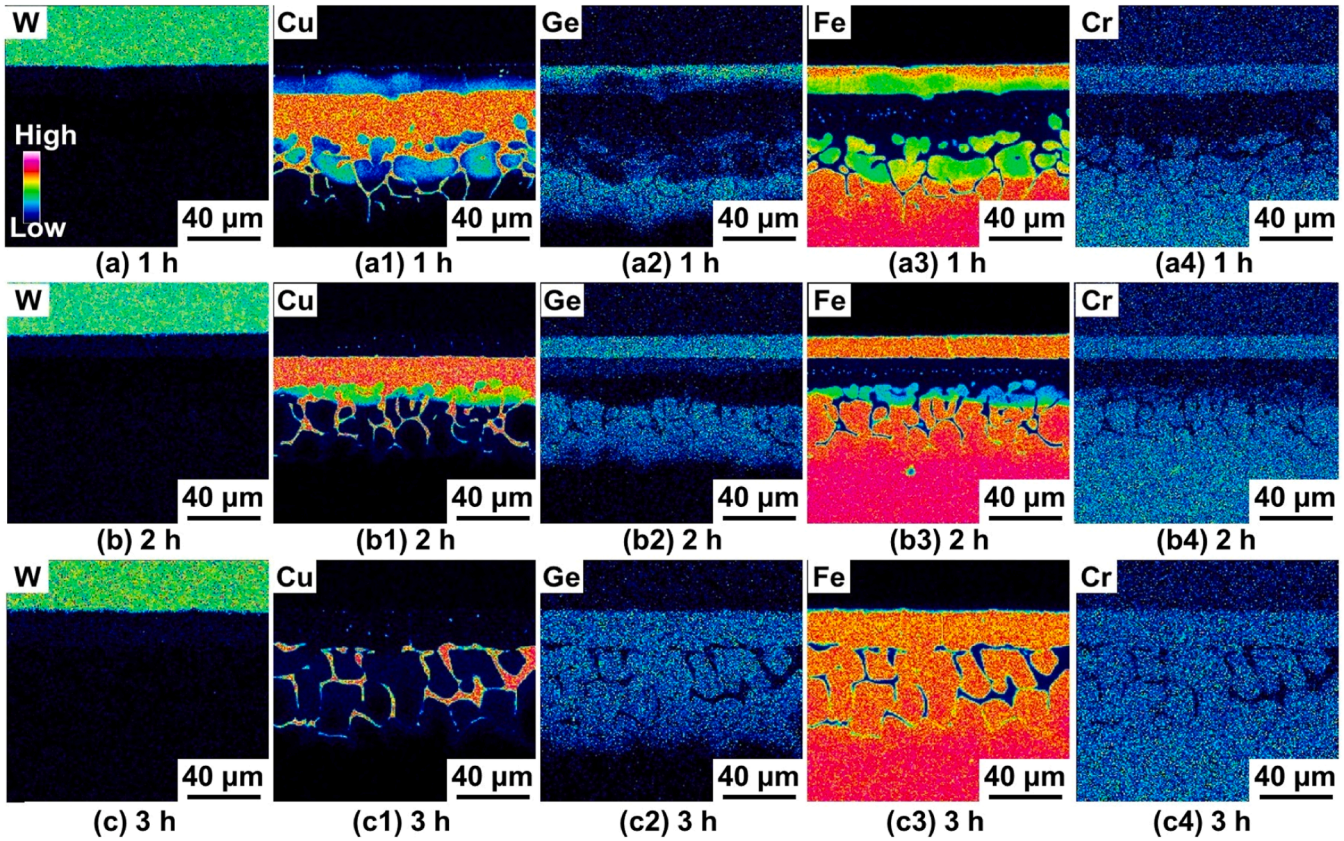


**Fig. 6.** EPMA elemental distribution maps of the single-side joints held different time. (a-a4) Holding 1 h, (b-b4) holding 2 h, (c-c4) holding 3 h.

were consistent with the structural characteristics obtained by SEM results in Fig. 5 and EPMA results in Fig. 6. Moreover, IPF maps in Fig. 7 indicated that the Fe-rich deposition layer consisted of columnar BCC grains. Corresponding KAM maps revealed notably low dislocation densities within this layer. Adjacent to the martensite steel matrix, a ferritic region developed, which could be attributed to the presence of Ge as a strong ferrite-forming element [30].

High-magnification SEM, EBSD and TEM analyses of the whole W/Fe-rich deposition layer interface held 3 h are displayed in Fig. 8. The interface comprised two distinct phases: 1-μm serrated $Fe_2W$ IMCs and nanoscale FCC grains with random crystallographic orientation, as shown in Figs. 8(a-a3). Figs. 8(b) and (b1) show FIB-SEM images for TEM analysis. The STEM/EDS maps in Figs. 8(d-d5) confirmed that the $Fe_2W$ phase contained W, Cr, Fe, Ge, and Cu, consistent with prior EPMA

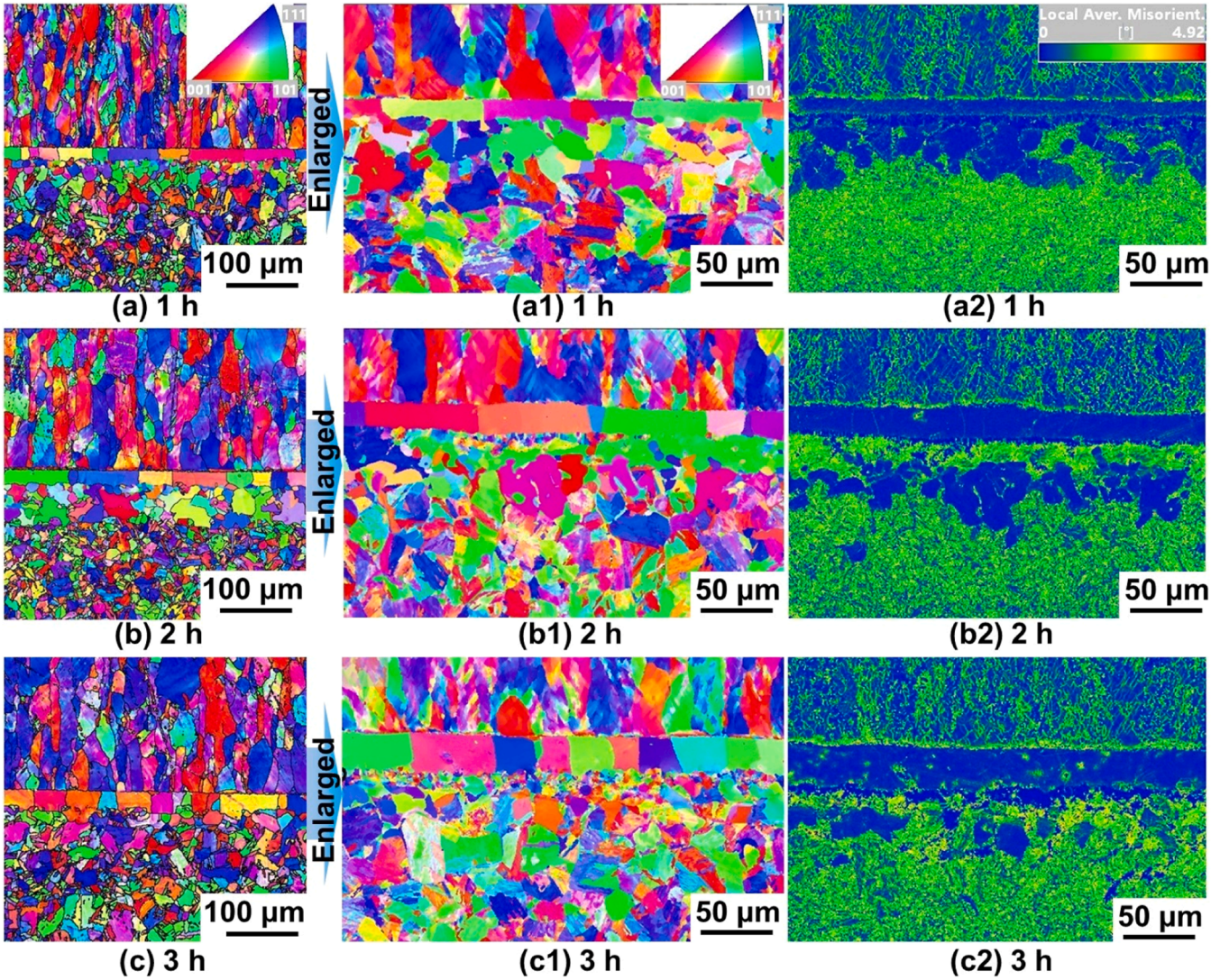


**Fig. 7.** (a-c) Typical EBSD IPF maps, (a1-c1) corresponding enlarged inverse pole figure (IPF) maps and (a2-c2) corresponding kernel average misorientation (KAM) maps of joints held different time: (a, a1, a2) holding 1 h, (b, b1, b2) holding 2 h, (c, c1, c2) holding 3 h.

data. Additionally, the individual FCC grains in Fig. 8(a1) were pure Cu. The random distribution of these nanometer-sized Cu grains may coordinate deformation of the W/Fe interface.

Fig. 9(a-a5) displays the morphology and crystallographic features of the W/Fe interface. SAED analysis further confirmed the serrated interfacial phase corresponds to $Fe_2W$, exhibiting a 5.66 % lattice distortion relative to ideal $Fe_2W$ (calculated from interplanar spacing difference of the same crystal plane between the ideal and experimental $Fe_2W$). This lattice distortion arose from the solid solution of Cr, Ge, and Cu. A well-defined orientation relationship existed between $Fe_2W$ and the W substrate: $(200)_W$ // $(20\bar{2}\bar{1})_{Fe2W}$, $[011]_W$ // $[01\bar{1}2]_{Fe2W}$. The lattice mismatch between the W matrix and the $Fe_2W$ phase was quantified using the following Eq. (2) [31]:

$$\delta = \left|\frac{\sigma_p - \sigma_m}{\sigma_m}\right| \quad (2)$$

where δ is the lattice mismatch between the W matrix and $Fe_2W$, $\sigma_p$and $\sigma_m$ are the plane spacing of the $Fe_2W$ and W matrix respectively. The measured interplanar spacings of the $(20\bar{2}\bar{1})$ plane in $Fe_2W$ (2.187 Å) and the (200) plane in W matrix (2.067 Å) yielded a mismatch (δ) of 5.49 % via Eq. (2), consistent with a semi-coherent W/Fe interface. The $Fe_2W$ phase exhibited periodic sharp stripe in Figs. 9(b-b2), and the elongated diffraction spots in SAED pattern in Fig. 9(b3), confirming extensive stacking faults (SFs) [32]. At the $Fe_2W$/Fe interface in Figs. 9 (c-c5), FCC pure Cu grains were observed.

Fig. 10 presents the interfacial hardness distribution of joints subjected to varying holding time. There was a significant hardness difference between W and steel base metals. The Fe-rich directional deposition layer consistently exhibited lower hardness than both base metals, suggesting its capacity to mitigate interfacial stress. With extended holding time, the hardness distribution of W/steel interface became more uniform, thereby avoiding abrupt hardness changes and mitigating the mismatch in thermal expansion coefficients between W and steel.

Fig. 11 shows the shear strength of joints under held for 1, 2 and 3 h. Strength increased progressively with extended duration, reaching 140 MPa for the joint held 1 h and 270 MPa for the joint held 2 h. When held for 3 h, the joint achieved a strength of 380 MPa, which was significantly higher than shear strengths of W/steel joints reported in previous studies, as illustrated in Fig. 11(b) [6,33–44]. Such enhanced strength would be crucial for improving the service life of W/steel joints in fusion reactor environments under thermal cycling.

Fig. 12 displays fracture morphologies of shear samples across holding time. In most recent studies on W-steel joints, shear failures in directly bonded W/steel joints predominantly occurred at the W/steel

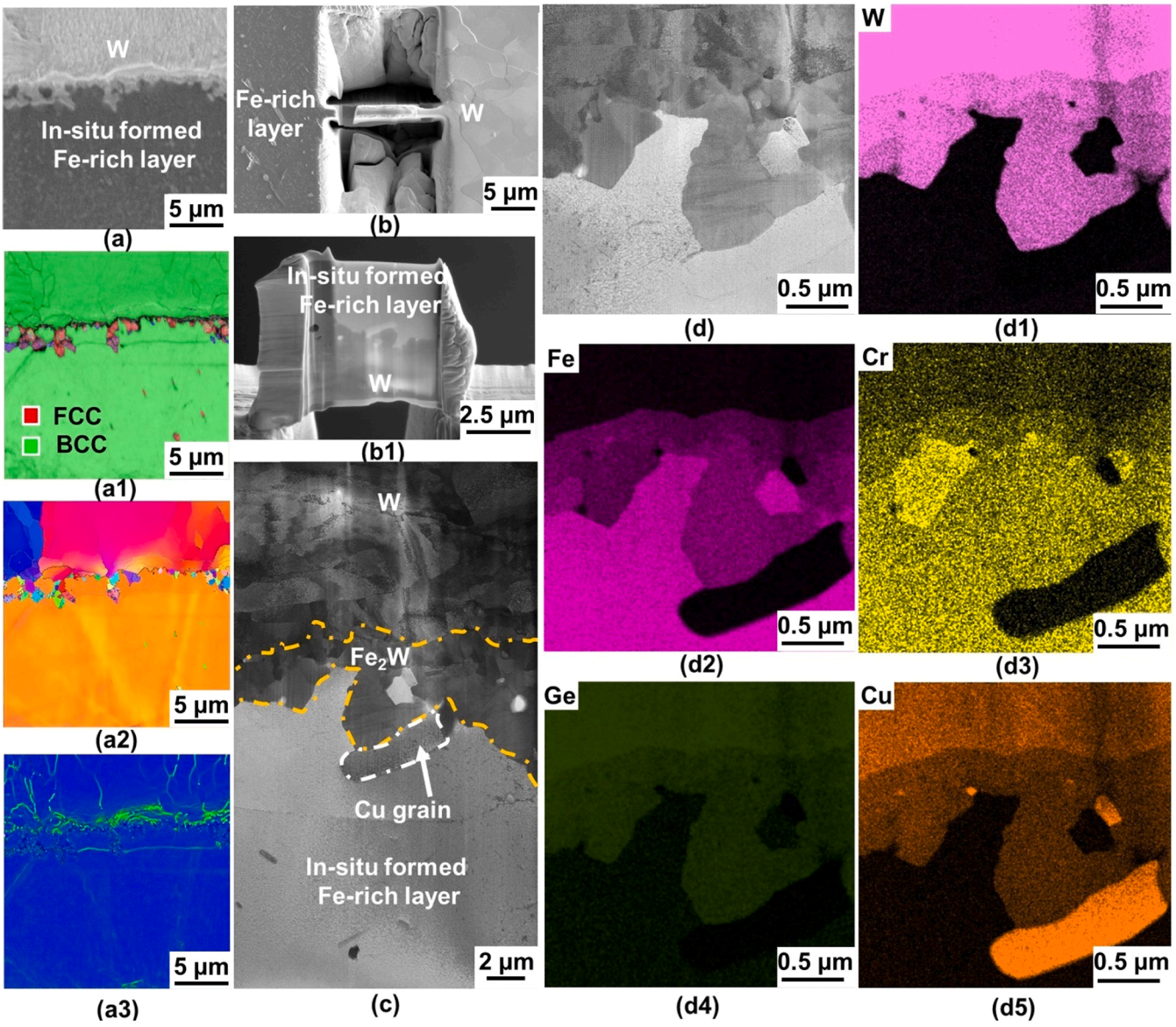


**Fig. 8.** (a-a3) SEM and EBSD maps of the W/Fe interface held 3 h. (a) The SEM map, (a1) the phase map, (a2) the IPF map, (a3) the KAM map. (b, b1) FIB-SEM image. (c) dark-filed image, (d-d5) STEM and EDS map analysis.

interface, while fracture surfaces in W/Cu interlayer/steel joints were predominantly observed at the W/Cu interface. However, in this study, by employing metallurgical transitional bonding and in-situ modification of $Fe_2W$, the low-strength issues at both the W/Cu and W/Fe interfaces were effectively resolved. Specifically, fractures of samples held 1 h and 2 h occurred in the Cu interlayer. Under shear loading, low-strength Cu interlayer underwent plastic deformation and failed first. Fracture surface EDS analysis confirmed that fracture occurred primarily within the pure Cu layer, with a minority of fractures located at the Cu/steel interface. Due to strengthened interfacial reactions and the reduced thickness of the pure Cu layer, the shear strength of joints held for 2 h was significantly higher than that of the samples held for 1 h. Crucially, the shear fracture location of the sample held 3 h extended across the Fe-rich deposition layer, indicating that the transformation of Cu from a singular interlayer to a reticulate heterostructure significantly enhanced the joint strength. Under shear loading, the Cu/steel reticulate heterostructure underwent coordinated deformation first. As the load increased, the thickened Fe-rich deposition layer also participated in deformation. Ultimately, fracture propagated across the entire composite interface, resulting in the highest shear strength. Fracture surfaces of samples subjected to different holding times predominantly exhibited brittle fracture characteristics. However, partially elongated parabolic dimples were consistently observed. This morphology arose because the shear load was transmitted parallel to the composite interface, causing the dimples to elongate and even deform into a parabolic shape.

## 4. Discussion

Microstructural characteristics, particularly elemental distributions and interface architectures, influence the mechanical performance of joints. While conventional pure Cu interlayers in W/steel joints mitigated thermal stress and prevent direct W/Fe contact, they inherently introduce mechanical vulnerabilities: non-metallurgical W/Cu bonding inherently limited joint strength [45].

In this study, a Cu-Ge alloy filler was developed to fabricate a novel W/steel joint with superior metallurgical bonding through in-situ element-selective directional diffusion. By constructing an Fe-rich deposition layer, the non-metallurgically bonded W/Cu interface was transformed into metallurgical-bonded W/Fe and Fe/Cu interfaces. In situ modification of the $Fe_2W$ phase suppressed its intrinsic brittleness

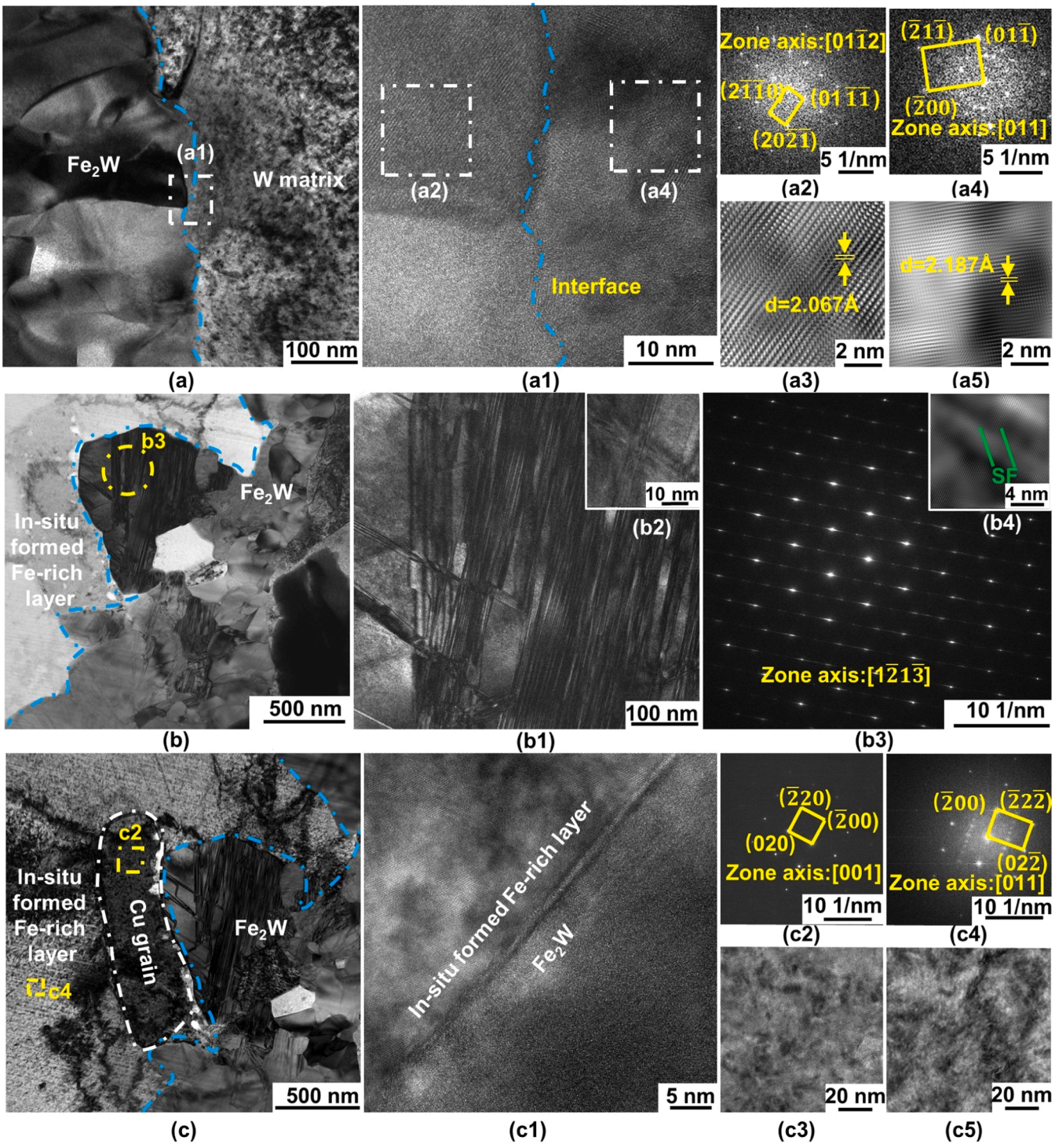


**Fig. 9.** TEM images of the W/Fe interface of joints held 3 h. (a-a5) The W/$Fe_2W$ interface: (a) dark-filed image, (a1) HRTEM image, (a2-a5) fast Fourier transform (FFT) and inverse fast Fourier transform (IFFT) patterns of areas marked in (a1). (b-b4) The analysis of $Fe_2W$ phase: (b-b2) dark-filed image, (b3) SAED patterns of areas marked in (b) and (b4) the corresponding HRTEM image. (c-c5) The $Fe_2W$/Fe-rich deposition layer interface: (c) dark-filed image, (c1) HRTEM image, (c2) SAED patterns of the Cu grain marked in (c), (c3) HRTEM of the Cu grain, (c4) FFT and IFFT patterns of the Fe-rich deposition layer, (c5) HRTEM of the Fe-rich deposition layer.

and significantly improved the W/Fe interface strength. Furthermore, structural evolution of the Cu interlayer from continuous layer to discontinuous reticulate heterostructure with steel improved the Cu/steel bonding strength. Therefore, further investigation was required to clarify the formation mechanisms of the unique multilayer metallurgical interfaces and their impact on mechanical properties of joints.

### *4.1. The in-situ formation mechanism of superior multilayer metallurgical bonding*

#### *4.1.1. The formation mechanism of Fe-rich deposition layer*

This study employed a Cu-Ge filler to bond W and steel, where multi-physics fields (temperature and gravity) drove formation of an Fe-rich directional deposition layer at the W/Cu interface, as shown in Fig. 5.

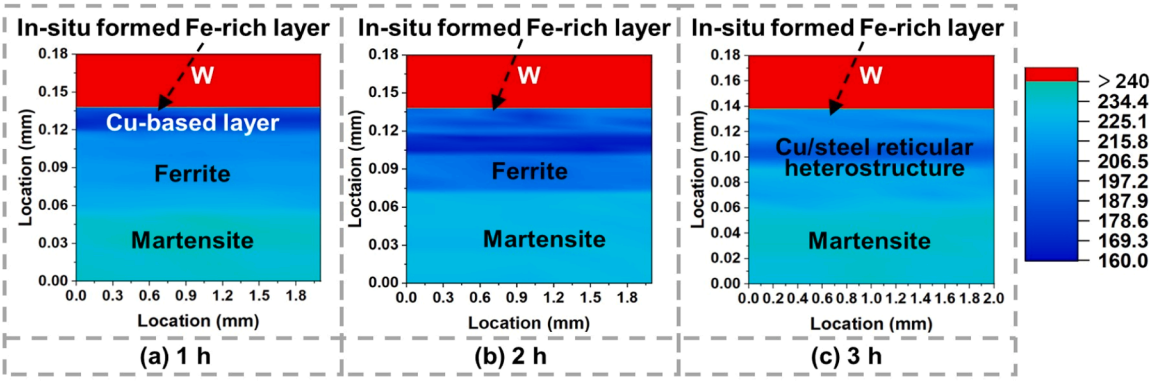


**Fig. 10.** Hardness cloud map of joints under different holding time: (a) 1 h, (b) 2 h and (c) 3 h.

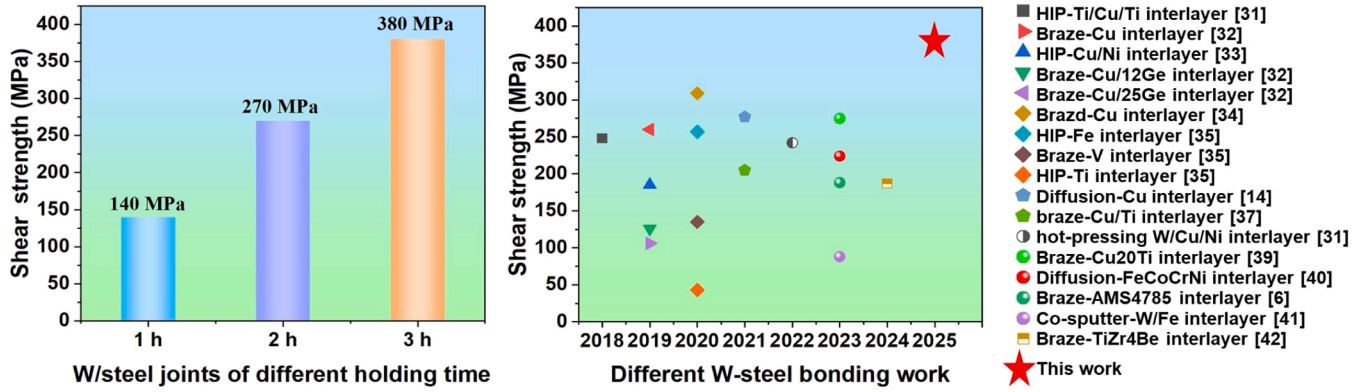


**Fig. 11.** (a) the shear strength of joints held 1, 2 and 3 h. (b) A comparison of shear strength between this work and other W/steel joint reported using different welding techniques [6,33–44].

Fig. 13 illustrates the underlying mechanism: synergistic temperature-gravity coupling governed in-situ element-selective directional diffusion. Upon heating to 850°C, the Cu-Ge filler metal melted, exhibiting enhanced wettability on the base metal and a reduced contact angle [16]. Ge alloying reduced the Cu solid-liquid transition temperature from 1080°C to 850°C, reduced the onset temperature of Fe-Cu reaction and enhanced Fe solubility in Cu [15]. Holding at 1040°C significantly improved the wetting behavior of molten Cu on steel while concurrently enhancing the thermodynamic driving force for Fe dissolution into the Cu melt. Additionally, the favorable solid solubility between Ge and Fe facilitated the diffusion and dissolution of Fe into the molten Cu. Moreover, Langevin dynamics (Eq. 3 [46]) and Navier-Stokes (Eq. 4 [47]) modeling revealed that gravitational potential energy dominated Fe atom trajectories in the liquid phase to enable directional deposition. At the W/steel interface positioned above the W substrate in Fig. 5(a), no Fe-rich deposition layer formed, the corresponding schematic is shown in Fig. 13(a). This absence confirmed gravitational potential energy gradients as the primary driver of Fe-rich deposition layer formation. Consequently, at the W/steel interface beneath the W substrate, lower-density particles (Fe, Cr, Ge) than Cu migrated directionally through the liquid Cu phase, depositing on the W side, corresponding schematic is shown in Fig. 13(b) and (c). The deposition of Fe and Cr atoms on the W side promoted the further diffusion of steel-side atoms into Cu melt, resulting in the formation of a thicker Fe-rich deposition layer as the holding time increased. This process was called in-situ element-selective directional diffusion.

$$m\frac{d^2x(t)}{dt^2} = -\nabla U(x(t)) - \gamma\frac{dx(t)}{dt} + \sqrt{2k_BT\gamma}R(t) \tag{3}$$

Where m is the mass of particles, $x(t)$ is the position of particles at time t, and $U(x(t))$ is the potential energy of particles at position $x(t)$, $\gamma$ is the friction coefficient, $k_B$ is the Boltzmann constant, T is the system temperature, and $R(t)$ is a Gaussian white noise term with zero mean and unit variance (random force).

$$v = \frac{2g(p_m - p_B)r^2}{9\eta} \tag{4}$$

where $v$ is the ascent velocity of the inclusions within the liquid phase, $r$ is the radius of the inclusions, $p_m$ is the liquid phase density, $p_B$ is the inclusions density, $g$ is the gravitational acceleration, and $\eta$ is the dynamic viscosity of the liquid phase.

First-principles calculations confirmed superior stability of the W/Fe interface versus W/Cu. Upon deposition, Fe preferentially reacted with W to form $Fe_2W$. Critically, in contrast to traditionally brittle $Fe_2W$, the $Fe_2W$ phase in this study alloyed by Cr, Ge, and Cu exhibited 5.66 % lattice distortion and extensive SFs, as shown in Figs. 9(b-b4). While HCP $Fe_2W$ intrinsically exhibited high Peierls barriers limiting dislocation slip, solute doping reduced these barriers [48], enhancing slip system mobility. Consequently, under interfacial thermal stress, the modified $Fe_2W$ accommodated strain through massive SFs formation via dislocation slip [49,50]. The observed lattice distortion and SFs confirmed successful in-situ modification of the $Fe_2W$ phase.

#### *4.1.2. The in-situ formation mechanism of the Cu/steel reticulate heterostructure*

After Cu-Ge filler melting, Ge either diffused into the steel or co-deposited with Fe and Cr on the W side. Crucially, Cu distribution characteristics evolved dynamically across holding time: prolonged processing transformed the original continuous Cu/steel interface into a discontinuous reticulate heterostructure, corresponding schematic is

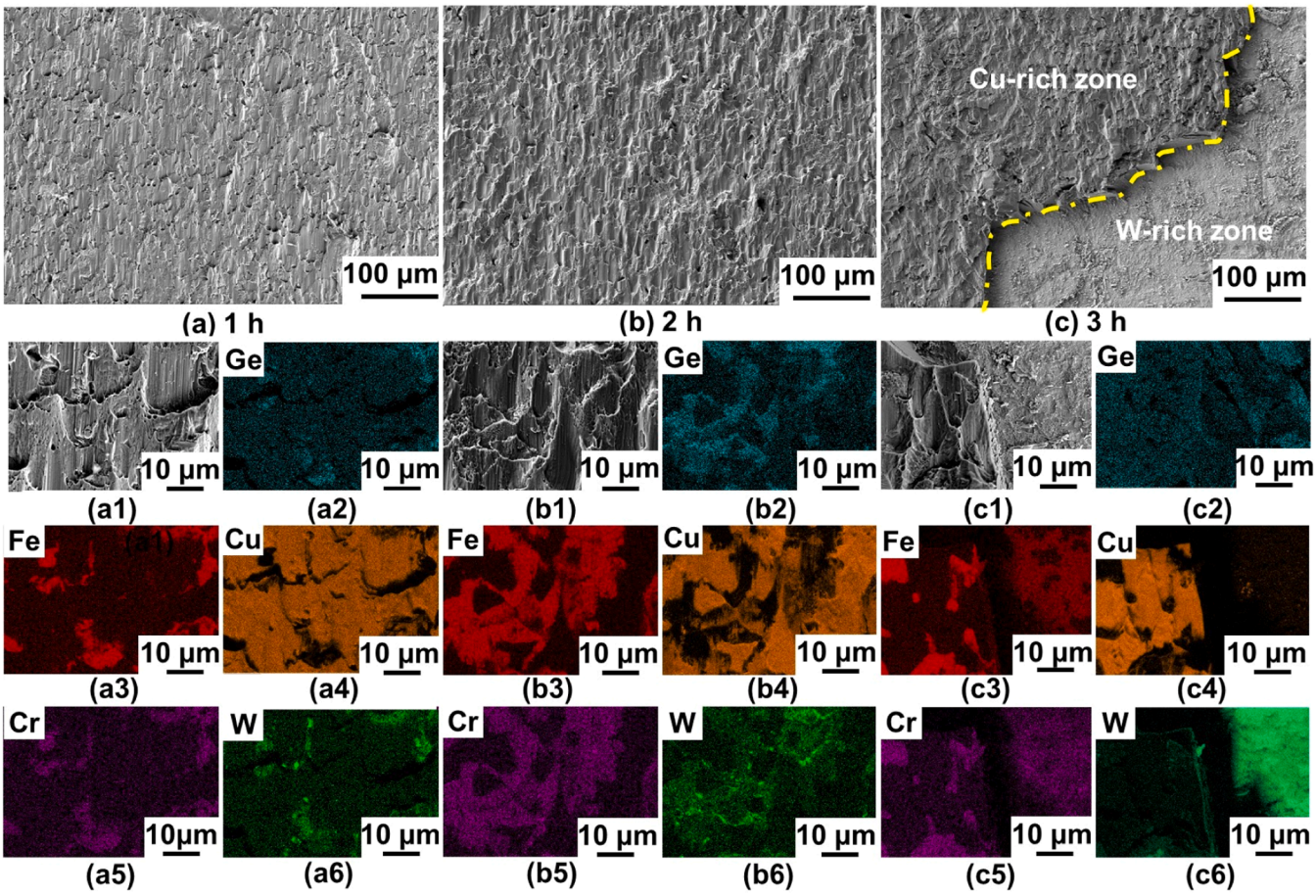


**Fig. 12.** The SEM and EDS elemental maps of shearing fracture surface of joints held at: (a-a6) 1 h, (b-b6) 2 h and (c-c6) 3 h.

shown in Fig. 13(b) and Fig. 13(c). This Cu/steel reticulate heterostructure originated from Cu-Fe special grain boundaries diffusion behavior. Grain boundaries had higher energy and lower diffusion activation energy compared to the intragranular [51], thereby providing preferential diffusion channels for Cu segregation into steel. Insufficient holding time produced incomplete boundary diffusion, yielding a continuous Cu interlayer upon solidification, as shown in Fig. 5(b-d). Extended durations of 3 h enabled Cu completely diffused and aggregated along the steel grain boundaries, resulting in the formation of the discontinuous Cu/steel interfacial heterostructure.

### *4.2. The effect of superior multilayer metallurgical interfaces on joint strength*

#### *4.2.1. The effect of Fe-rich deposition layers on joint strength*

Conventional W/steel joints with a Cu interlayer failed at the weakly bonded W/Cu interface. This study overcame this limitation by creating metallurgical W/Fe/Cu interfaces through in-situ formation of an Fe-rich deposition layer, as shown in Fig. 13(d) and Fig. 13(e). Notably, traditionally W/Fe interface risked brittle $Fe_2W$ intermetallic failure, but the high-strength W/Fe interface was achieved for the first time in this work. This enhanced interfacial strength was partially attributed to the semi-coherent W/$Fe_2W$ interface. The $Fe_2W$ phase exhibited a defined orientation relationship with the W matrix: $(200)_W$ // $(20\bar{2}1)_{Fe2W}$, $[011]_W$ // $[01\bar{1}2]_{Fe2W}$, as shown in Fig. 9(a2-a5). This orientation relationship indicated that $Fe_2W$ preferentially grew along (200) and $(\bar{2}00)$ planes of the W matrix, establishing a semi-coherent interface with 5.49 % lattice mismatch. This crystallographic alignment effectively reduced interfacial energy, mitigated lattice mismatch at the phase boundary, alleviated interfacial stress [52]. In-situ modification of $Fe_2W$ IMCs represented another critical factor enabling the high-strength W/Fe interface, because conventional brittle $Fe_2W$ compromised W/steel joint strength. This embrittlement primarily arose from bonding defects within $Fe_2W$, specifically in the internal W-Fe or W-W atomic bonds [53]. In addition, the HCP $Fe_2W$ exhibited low crystal symmetry, insufficient slip systems, small atomic spacing on slip planes, and strong interatomic binding forces, collectively increasing Peierls-Nabarro stress required for dislocation motion [54]. Consequently, conventional $Fe_2W$ IMCs typically reached failure stress before dislocation slip initiated under load, triggering brittle cracking. In this study, however, Cr, Cu, and Ge alloying modified the $Fe_2W$ composition, inducing lattice distortion that stabilized chemical bonding and enhanced atomic cohesion [55]. Concurrently, SFs formation within $Fe_2W$ also represented a manifestation of modifying its intrinsic brittleness. Due to the mismatch in CTE, thermal stress accumulated at the W/Fe interface during welding, posing a risk of interfacial cracking [56]. In this study, SFs generation within $Fe_2W$ actively relieved W/Fe interfacial thermal stresses. Xu et al. had similarly noted that SFs in $Al_4C_3$ IMCs released interfacial stress under thermal loading [57]. Furthermore, Zhang et al. [58] established that mechanically seeding dislocations into the intrinsically brittle hard phase could enhance its plasticity and toughness enhancement by triggering profuse dislocation multiplication via cross slip and motion. In addition, the termination of SFs within the crystal necessarily resulted in the formation of partial Shockley or Frank dislocations at their boundaries [59]. Therefore, the SFs existing within $Fe_2W$ contributed significantly to its plasticization and toughening. These SFs reduced the dislocation nucleation barrier while simultaneously promoting cross-slip and dislocation motion. This mechanism aligned with observations by Wu et al. [32], who observed SFs as the primary deformation mode at room temperature in

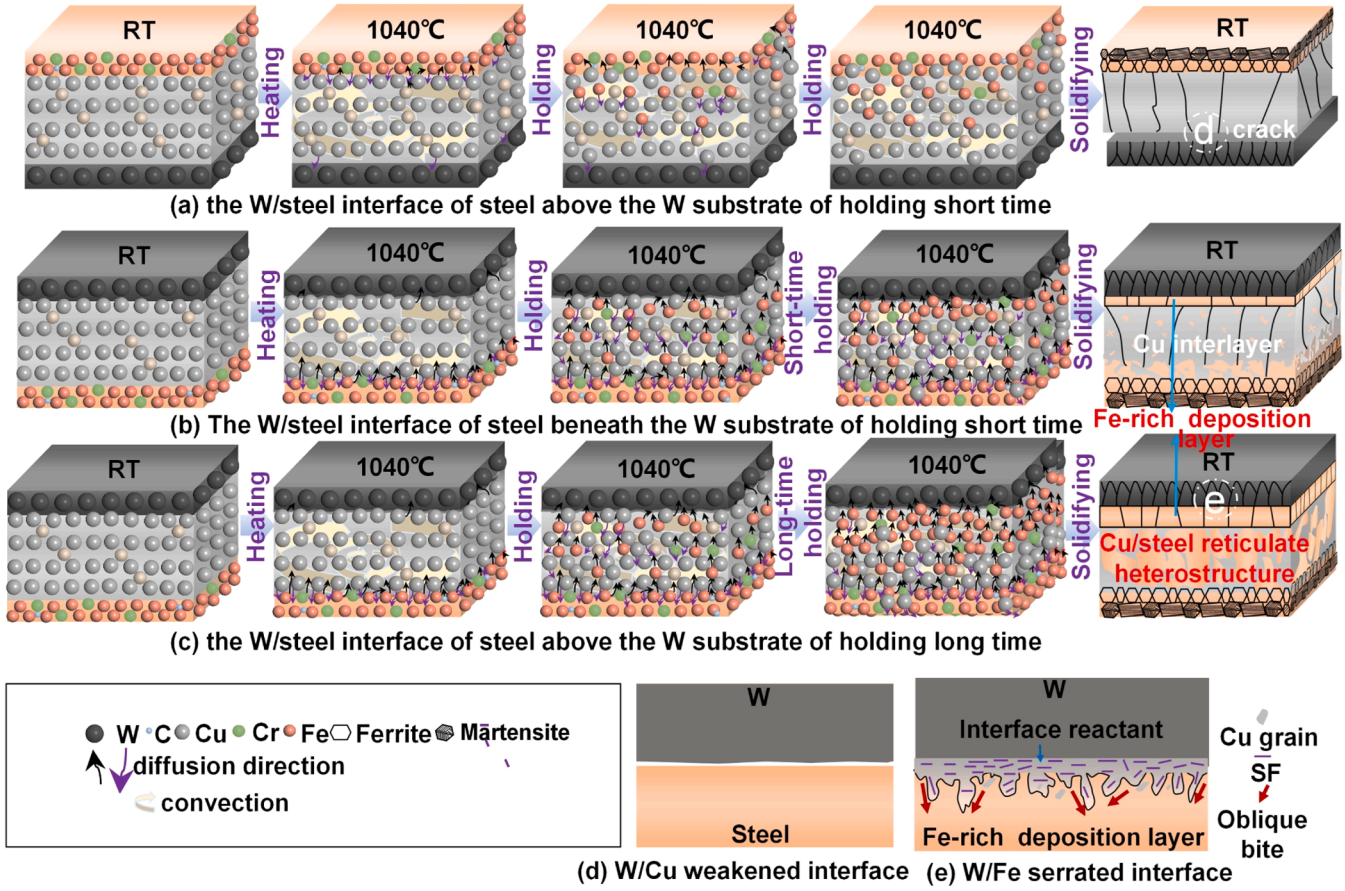


**Fig. 13.** Schematic diagram of W/Steel joint with multilayer metallurgical interfaces.

multicomponent alloys. Furthermore, the nanometer-scale serrated morphology of $Fe_2W$ enhanced bonding effectiveness and crack resistance through mechanical interlocking and oblique interdigitation [60].

Ultimately, the W/Fe bonding was substantially enhanced by the W/$Fe_2W$ interface coherence and the in-situ modification of $Fe_2W$ IMCs.

*4.2.2. The effect of Cu/steel reticulate heterostructure on the joint strength*

A continuous Cu/steel interface formed during insufficient holding time, as shown in Fig. 5(b), (c) and (d) and Fig. 6. Shear fractures of samples held 1 h and 2 h occurred at this interface, indicating relatively low interfacial strength. With increased holding time (3 h), a discontinuous reticulate structure developed, as shown in Fig. 5(e) and Fig. 6. Subsequent shear fractures spanned through the Fe-rich deposition layer instead of the Cu/steel interface, demonstrating that the discontinuous reticulate heterostructure significantly enhanced interfacial strength. This improvement arose partly because the soft Cu phase surrounding the ferrite preferentially deformed, mitigating high thermal stresses induced during W/steel processing and preparation [61]. Concurrently, this reticulate heterostructure coordinated deformation and alleviated stress concentration, thereby significantly enhancing the fracture toughness of the Cu/steel interface [62]. Furthermore, this heterostructure enabled partially direct bonding regions between the steel substrate and the Fe-rich deposition layer, enhancing metallurgical bonding of the joint. Attribute to these synergistic effects, the optimal joint held 3 h exhibited superior mechanical performance.

## 5. Conclusions

In the present work, addressing the issue of low strength in traditional W/steel joints utilizing Cu interlayers, a novel approach was proposed to fabricate a W/steel joint with superior multilayer metallurgical bonding. This is achieved by constructing an Fe-rich directional deposition layer at the W/Cu interface and a reticulate heterostructure at the Cu/steel interface. The formation mechanisms and their influence on mechanical performance were systematically investigated and discussed. The major findings are summarized as follows:

(1) By introducing Cu-Ge interlayers at W/steel joints, Fe and Cr elements from the steel side migrated across the Cu-based interlayer and directional in-situ deposited on the W side, forming an Fe-rich deposition layer via adjusting elemental diffusion behavior, controlling interfacial liquid-solid reactions and utilizing multi-physics fields. This process successfully transformed the traditional non-metallurgical W/Cu bonding into metallurgical W/Fe and Fe/Cu bonding.

(2) A high-strength W/Fe interface was achieved through in-situ toughening of brittle $Fe_2W$ phases and the formation of semi-coherent W/$Fe_2W$ interface with the orientation relationship ($(200)_W$ // $(20\bar{2}1)_{Fe2W}$, $[011]_W$ // $[01\bar{1}2]_{Fe2W}$). These brittle $Fe_2W$ phases were modified via lattice distortion and SFs formation during via multi-element (Cr, Ge, and Cu) alloying.

(3) Under sufficient solid-liquid interface reaction, a discontinuous reticulate heterostructure formed at the Cu/steel interface, with Cu along the steel grain boundaries. This heterostructure enhanced the joint performance by releasing stress concentration through preferential Cu deformation and optimizing the distribution of soft pure Cu.

(4) The inherent limitations of conventional low-strength W/Cu and Cu/steel joining were resolved through in-situ element-selective directional diffusion. This approach successfully developed a novel W/steel joint with exceptional interfacial bonding strength,

achieving a shear strength of 380 MPa, which significantly surpassed that reported in all current relevant studies.

This work elucidates the mechanisms of interfacial metallurgical bonding, strengthening, and in-situ modification of brittle phases in dissimilar metal joints with significant thermophysical property differences. It provides a novel pathway for high-strength metallurgical joining of dissimilar metals in harsh service environments and offers new insights into the modification and toughening of brittle phases at welded interfaces. Future work will focus on constructing continuous gradient-transition metallurgical joints via in-situ element-selective directional diffusion strategy, effectively matching CTE between base metal and avoiding dissimilar interfaces.

## CRediT authorship contribution statement

**Wang Ji-chao:** Writing – review & editing, Methodology, Data curation. **Xiaonan Qi:** Writing – review & editing, Methodology, Data curation. **Guangnan Luo:** Supervision, Resources, Conceptualization. **Wanjing Wang:** Writing – review & editing, Supervision, Conceptualization. **Huaqi Xu:** Writing – review & editing, Writing – original draft, Investigation, Formal analysis, Data curation. **Ming-Hsien Lee:** Validation, Software, Methodology. **Wenjing Zhang:** Writing – review & editing, Supervision, Conceptualization. **Wei Liu:** Writing – review & editing, Supervision, Resources, Funding acquisition, Conceptualization. **Yuping Xu:** Supervision. **Haishan Zhou:** Supervision, Methodology, Conceptualization. **Shubo Zhang:** Methodology, Investigation, Formal analysis. **Mingshen Li:** Methodology, Investigation, Data curation. **Ye Jiao:** Writing – review & editing, Formal analysis. **Kailun Li:** Methodology, Investigation, Data curation.

## Declaration of Competing Interest

The authors declare that they have no known competing financial interests or personal relationships that could have appeared to influence the work reported in this paper.

## Acknowledgments

This work is supported by the National Magnetic Confinement Fusion Energy R&D Program of China under contract number 2019YFE03130003, the National Natural Science Foundation of China (Nos. 52275391), the China United Gas Turbine Technology Co., Ltd under the project of J790, and HuaMi Innovation and Venture Fund.

## Appendix A. Supporting information

Supplementary data associated with this article can be found in the online version at doi:10.1016/j.jmatprotec.2025.119064.

## Data Availability

Data will be made available on request.

## References

[1] Gruber, O., Sips, A.C.C., Dux, R., Eich, T., Fuchs, J.C., Herrmann, A., Kallenbach, A., Maggi, C.F., Neu, R., Pütterich, T., Schweinzer, J., Stober, J., 2009. Compatibility of ITER scenarios with full tungsten wall in ASDEX upgrade. Nucl. Fusion 49 (11).
[2] Zhang, X., Wu, Q., Du, H., Zheng, Y., Lu, P., Liu, S., 2022. Activation analysis and radwaste assessment of CFETR. Fusion Eng. Des. 176, 113036.
[3] Müller, Av, Dorow-Gerspach, D., Balden, M., Binder, M., Buschmann, B., Curzadd, B., Loewenhoff, T., Neu, R., Schlick, G., You, J.H., 2022. Progress in additive manufacturing of pure tungsten for plasma-facing component applications. J. Nucl. Mater. 566.
[4] Huang, P., Wang, Y., Peng, H., Chen, J., Wang, P., 2020. Diffusion bonding w and RAFM-steel with an fe interlayer by hot isostatic pressing. Fusion Eng. Des. 158.
[5] Basuki, W.W., Aktaa, J., 2011. Investigation on the diffusion bonding of tungsten and EUROFER97. J. Nucl. Mater. 417 (1-3), 524–527.
[6] Singh, K.P., Patel, A., Bhope, K., Rimza, S., Mehta, M., Khirwadkar, S.S., 2023. High temperature vacuum brazing of tungsten to tungsten alloy with structural material. Fusion Eng. Des. 197.
[7] Peng, L., Mao, Y., Zhang, Y., Xi, L., Deng, Q., Wang, G., 2018. Microstructural and mechanical characterizations of W/CuCrZr and w/steel joints brazed with Cu-22TiH 2 filler. J. Mater. Process. Technol. 254, 346–352.
[8] Loewenhoff, T., Bardin, S., Greuner, H., Linke, J., Maier, H., Morgan, T.W., Pintsuk, G., Pitts, R.A., Riccardi, B., De Temmerman, G., 2015. Impact of combined transient plasma/heat loads on tungsten performance below and above recrystallization temperature. Nucl. Fusion 55 (12).
[9] Wang, Z., Zhang, S., Xu, J., Zhang, Z., Shao, W., Zhao, Y., Huang, J., Chen, S., Ye, Z., Wang, W., Yang, J., 2025. Investigation on enhanced strength in W/(Ti/Cu) composite interlayer/steel diffusion bonding joint based on controlled diffusion mechanism. J. Mater. Process. Technol. 343, 118978.
[10] Zhang, J., Xie, D., Li, Q., Jiang, C., Li, Q., 2020. Effect of holding time on the microstructure and strength of tungsten/steel joints by HIP diffusion bonded using a cu interlayer. Mater. Lett. 261.
[11] Zhang, J., Huang, Y., Liu, Y., Wang, Z., 2018. Direct diffusion bonding of immiscible tungsten and copper at temperature close to copper's melting point. Mater. Des. 137, 473–480.
[12] Zhang, J., Yu, L., Liu, Y., Liu, C., Ma, Z., Li, H., Wang, Z., Long, D., 2022. Stable bonding of w and ODS steel fabricated by TLP diffusion technology through inserting a novel composite interlayer Zr/Cu. J. Mater. Process. Technol. 299, 117341.
[13] Chaubey, A.K., Gupta, R., Kumar, R., Verma, B., Kanpara, S., Bathula, S., Khirwadkar, S.S., Dhar, A., 2018. Fabrication and characterization of W-Cu functionally graded material by spark plasma sintering process. Fusion Eng. Des. 135, 24–30.
[14] Chu, Q., Li, Y., Cao, Q., Zhang, M., Zhao, P., Yan, F., Luo, H., Wang, X., Yan, C., 2022. Microstructure and mechanical properties of cu/steel dissimilar joints. Int. J. Press. Vessels Pip. 200, 104828.
[15] Zhai, W., Geng, D.L., Wang, W.L., Wei, B., 2012. A calorimetric study of thermodynamic properties for binary Cu–Ge alloys. J. Alloy. Compd. 535, 70–77.
[16] Janusz-Skuza, M., Bigos, A., Valenza, F., Gambaro, S., Bieda, M., Trybula, M.E., Wojewoda-Budka, J., 2025. Dissolution wetting of liquid copper on steel substrate – phenomena occurring during liquid-solid interaction. Mater. Charact. 223.
[17] Luna, F.D.T., Silva, A.G., Fukumasu, N.K., Bazan, O., Gouveia, J.H.A., Moraes, D., Yanagihara, J.I., Vianna, A.S., 2019. Fluid dynamics in continuous settler. Chem. Eng. J. 362, 712–720.
[18] Huang, S., Lin, B., Niu, W., Wang, G., Li, J., 2025. Study on the microstructure evolution and mechanical properties of spray-forming Cu-Fe alloys with varying fe compositions. J. Alloy. Compd. 1013, 178452.
[19] Zhang, B., Chang, Q., Sun, Z., Li, D., Pan, H., Zhang, L., 2022. A concept of regulating the distribution of continuous brittle phases by spatial division of the Ti3SiC2/Ti2AlNb brazing seam. Mater. Des. 221.
[20] Chen, Y., Zhang, H., Zhu, Z., Xu, G., Luo, A.A., Liu, L., 2019. Inhibiting brittle intermetallic layer in Magnesium/Aluminum bimetallic castings via in situ formation of Mg2Si phase. Metall. Mater. Trans. B 50 (4), 1547–1552.
[21] Wang, J.-C., Wang, W., Li, Q., Qin, S., Lei, M., Luo, G.-N., 2021. A method for high heat flux fatigue test of W/Cu/steel small mock-up using normal cooling conditions. Nucl. Mater. Energy 28.
[22] J.P. Fackler, R.J. Staples, R.G. Raptis, First principles methods using CASTEP, 2005, 220, pp. 5-6.
[23] Gauthier, V., Robaut, F., Upadhyaya, A., Allibert, C.H., 2003. Effect of fe on the constitution of Cu–W alloys at 1200 °C. J. Alloy. Compd. 361 (1-2), 222–226.
[24] Jacob, A., Schmetterer, C., Singheiser, L., Gray-Weale, A., Hallstedt, B., Watson, A., 2015. Modeling of Fe–W phase diagram using first principles and phonons calculations. Calphad 50, 92–104.
[25] Liu, Y., Jiang, Y., Zhou, R., Feng, J., 2014. First-principles calculations of the mechanical and electronic properties of Fe–W–C ternary compounds. Comput. Mater. Sci. 82, 26–32.
[26] Wu, Z., Pang, M., Zhan, Y., Shu, S., Xiong, L., Li, Z., 2021. The bonding characteristics of the Cu(111)/WC(0001) interface: an insight from first-principle calculations. Vacuum 191, 110218.
[27] Yuan, X., Xiao, Y., Wang, G., Zhang, L., 2021. TiN inducing ferrite nucleation based on the bcc-Fe/TiN interfaces formation at atomic scale by first-principles calculation. Comput. Mater. Sci. 197, 110570.
[28] Li, J., Chen, D., Fan, T., Hu, X., Rong, H., Zheng, Z., Zheng, H., Liu, C., 2022. Investigation on TaC (1 1 1)/TiC (1 1 1) interface for coating with high-performancse corrosion resistance: First-Principle calculations and experiments. Appl. Surf. Sci. 605.
[29] Mac Donald, B.J., Hashmi, M.S.J., 2001. Three-dimensional finite element simulation of bulge forming using a solid bulging medium. Finite Elem. Anal. Des. 37 (2), 107–116.
[30] Xu, H., Wang, W., Wang, J.-C., Zhang, W., Chen, Z., Qi, X., Jiao, Y., Zhang, S., Du, P., Wang, Q., Yu, Z., Xu, Y., Zhou, H., Liu, W., Luo, G.-N., 2024. Improving the interface strength and fatigue property of W-Cu-steel brazed joint via induced interface alloying. J. Mater. Process. Technol. 332, 118535.
[31] Peng, W.-Q., Li, Q., Xu, Y.-P., Zhou, H.-S., Luo, G.-N., 2024. Achieving novel copper–steel joints with a combination of high strength and ductility reinforced by in-situ Fe-rich particles. J. Mater. Sci. Technol. 182, 231–245.
[32] Wu, P., Zhang, Y., Han, L., Gan, K., Yan, D., Wu, W., He, L., Fu, Z., Li, Z., 2023. Unexpected sluggish martensitic transformation in a strong and super-ductile high-entropy alloy of ultralow stacking fault energy. Acta Mater. 261.

[33] Liu, W., Pang, X., Cai, Q., Ma, Y., Zhu, W., 2018. Fabrication of w/steel joint using hot isostatic pressing with Ti/Cu/Ti liquid forming interlayer. Fusion Eng. Des. 135, 59–64.
[34] Bachurina, D., Suchkov, A., Filimonov, A., Fedotov, I., Savelyev, M., Sevryukov, O., Kalin, B., 2019. High-temperature brazing of tungsten with steel by Cu-based ribbon brazing alloys for DEMO. Fusion Eng. Des. 146, 1343–1346.
[35] Wang, J.-C., Huang, J., Sun, H., Wang, W., Li, Q., Xu, S., Qin, S., Liu, S., Luo, G.-N., Li, J., 2019. Effect of composite interlayer on bonding quality of w and steel HIP joint. Fusion Eng. Des. 149.
[36] de Prado, J., Sánchez, M., Ruiz, A., Ureña, A., 2020. Effect of brazing temperature, filler thickness and post brazing heat treatment on the microstructure and mechanical properties of W-Eurofer joints brazed with cu interlayers. J. Nucl. Mater. 533.
[37] Chen, J.M., Liu, X., Wang, P.H., Huang, P., Wang, J.B., Cai, L.Z., Jin, F.Y., Zhu, X. B., Li, Q., Chen, Y.Y., Wei, Z.X., Xu, M., Duan, X.R., 2020. Progress in developing ITER and DEMO first wall technologies at SWIP. Nucl. Fusion 60 (1).
[38] Sun, L., Song, X., Dong, Y., Zou, J., Li, X., Ni, L., Gao, L., Liang, S., 2021. Microstructure and strength of diffusion bonded 304 stainless steel/tungsten joints using different interlayers. J. Manuf. Process. 65, 428–434.
[39] Bachurina, D., Suchkov, A., Gurova, J., Savelyev, M., Dzhumaev, P., Kozlov, I., Svetogorov, R., Leont'eva-Smirnova, M., Sevryukov, O., 2021. Joining tungsten with steel for DEMO: simultaneous brazing by Cu-Ti amorphous foils and heat treatment. Fusion Eng. Des. 162.
[40] Yang, Z., Zhang, X., Cheng, J., Li, X., Shen, Y., 2022. Effect of bonding process on the microstructures and strength of w/steel joints with a W-Cu-Ni interlayer. Int. J. Refract. Met. Hard Mater. 106.
[41] Izaguirre, I., Loewenhoff, T., de Prado, J., Sánchez, M., Wirtz, M., Díaz-Mena, V., Ureña, A., 2023. Thermal fatigue response of W-EUROFER brazed joints by the application of high heat flux loads. J. Mater. Process. Technol. 319.
[42] Qi, Q., Ren, J., Yue, Y., Gu, Z., Zhu, Y., Wang, C., 2023. Benefits of high entropy alloy interlayer in the vacuum diffusion bonding of W-CLAM steel. Vacuum 214.
[43] Casalegno, V., Perero, S., Girman, V., Sedlák, R., Scarpellini, A., Dorow-Gerspach, D., Heuer, S., Ferraris, M., 2023. W/Fe co-sputtered layers for tungsten to steel joints. Nucl. Mater. Energy 35.
[44] Kirillova, V.O., Popov, N.S., Gurova, J.A., Bachurina, D.M., Tan, X., Fedotov, I.V., Suchkov, A.N., 2024. Brazing SMART tungsten alloys to RAFM steels by Titanium-Zirconium-Beryllium brazing alloy. Fusion Eng. Des. 201.
[45] Tian, N.-N., Zhang, C.-L., Lyu, P., Guan, J.-T., Cai, J., Guan, Q.-F., Guo, S., 2024. High-current pulsed electron beam modification on microstructure and performance of Cu/CuW diffusion bonding joints. Rare Met. 43 (6), 2819–2831.
[46] Olivares-Rivas, W., Colmenares, P.J., 2016. The generalized langevin equation revisited: analytical expressions for the persistence dynamics of a viscous fluid under a time dependent external force. Phys. A Stat. Mech. Appl. 458, 76–94.
[47] Katopodes, N.D., 2019. Chapter 5 - viscous fluid flow. In: Katopodes, N.D. (Ed.), Free-Surface Flow. Butterworth-Heinemann, pp. 324–426.
[48] Ma, D., Friák, M., von Pezold, J., Neugebauer, J., Raabe, D., 2015. Ab initio study of compositional trends in solid solution strengthening in metals with low peierls stresses. Acta Mater. 98, 367–376.
[49] Shih, M., Miao, J., Mills, M., Ghazisaeidi, M., 2021. Stacking fault energy in concentrated alloys. Nat. Commun. 12 (1).
[50] Yuan, L., Jiang, F.Y., Hao, D., Yang, Y.Z., Chou, T.H., Zhang, J.X., Gan, J., Li, J.L., Xiong, J.T., Yang, T., 2025. Ultrastrong and ductile superalloy joints bonded with a novel composite interlayer modified by high entropy alloy. J. Mater. Sci. Technol. 222, 152–163.
[51] Wei, M., Zhai, T., Wang, K., 2024. A study of grain boundary precipitation of nano-scale Cu-rich phase in polycrystalline Fe–Cu binary alloys using a phase-field method. J. Mater. Res. Technol. 33, 8983–8991.
[52] Yin, Q., Chen, G., Teng, X., Xiang, Y., Leng, X., 2024. Interfacial coherence regulation and stabilization of molybdenum/kovar alloy welded joint by CoCrCuFeNi high entropy alloy. J. Mater. Sci. Technol. 194, 43–50.
[53] Wang, Y., Chen, S., Yang, J., Huang, J., Chen, S., Ye, Z., 2022. Microstructure, properties, and formation mechanisms of tungsten/steel hot isostatic pressing diffusion bonding joint utilizing a Ni-Si-B interlayer. J. Mater. Process. Technol. 299.
[54] Tan, Y., Wang, J., Feng, F., Guo, J., Lian, Y., Liu, X., Du, J., Li, S., Zhao, T., Wu, C., Tang, J., 2024. Additive manufacturing of W/RAFM hypervapotron plasma-facing components and the steady state thermal fatigue behavior. J. Nucl. Mater. 601.
[55] Volkova, E.G., Kozlov, K.A., Antonov, B.D., Murzakaev, A.M., Zavalishin, V.A., Livinets, A.A., Yu, V.A., 2022. Alloying of Al2Au intermetallic compound with cu by the ball milling technique. J. Alloy. Compd. 900.
[56] Grammes, T., Emmerich, T., Qu, D., Heinze, O., Vaßen, R., Aktaa, J., 2023. Functionally graded tungsten/EUROFER coating for DEMO first wall: from laboratory to industrial production. Fusion Eng. Des. 188.
[57] Xu, T., Zhu, Z., Mi, G., Sing, S.L., Ma, X., 2023. Silicon nitride assisted carbon nanotubes induced stacking faults and twins in aluminum alloy composite joint. J. Mater. Res. Technol. 25, 6965–6976.
[58] Zhang, J., Fang, X., Lu, W., 2025. Impact of dislocation densities on the microscale strength of single-crystal strontium titanate. Acta Mater. 291.
[59] Wagner, C., George, E.P., Laplanche, G., 2025. Effects of grain size and stacking fault energy on twinning stresses of single-phase cr Mn20Fe20Co20Ni40- high-entropy alloys. Acta Mater. 282.
[60] Zhu, L., Zhou, Q., Song, C., Liu, L., Zhang, L., Fan, K., Zhang, Y., Lu, H., Hu, Q., Sheng, Z., Guo, Y., Liu, K., 2024. Microstructure and mechanical properties of T2 copper /316L stainless steel explosive welding composite with small size wavy interface. J. Mater. Res. Technol. 28, 668–682.
[61] Xiao, P., Zhao, Q., Sheng, Y., Yang, C., Gao, Y., Wu, W., Liu, Z., Yi, Y., 2023. Superior strength–toughness synergy of heterogeneous TiB2p/AZ91 composites containing hard/soft zones via tailoring bimodal grain structure. Mater. Sci Eng. A 887, 145775.
[62] Lin, Y., Wang, J., Hu, L., Zhang, L., Zhang, R., Yu, J., Wu, B., 2024. Improving strength-ductility balance of a brittle Al-doped FeCrNi multi-principal element alloy by introducing a heterostructure with hard phase enveloping soft phase. Intermetallics 175, 108542.